1-20-2021

A multi-modal approach to measuring particulate iron speciation in buoyant hydrothermal plumes

Brandy D. Stewart

Jeffry V. Sorensen

Kathleen Wendt

Jason B. Sylvan

Christopher R. German

See next page for additional authors

Recommended Citation

Stewart, Brandy D., et al. "A multi-modal approach to measuring particulate iron speciation in buoyant hydrothermal plumes." Chemical Geology 560 (2021): 120018. https://doi.org/10.1016/j.chemgeo.2020.120018

A multi-modal approach to unpacking iron biogeochemical processes in buoyant hydrothermal plumes

Brandy D. Stewart[1], Jeffry V. Sorensen[1], Kathleen Wendt[1,2], Jason B. Sylvan[3], Christopher R. German[4], Karthik Anantharaman[5,6], Gregory J. Dick[5], John A. Breier[7], Brandy M. Toner[1,*]

[1] Department of Soil, Water, and Climate, University of Minnesota – Twin Cities, St. Paul, MN 55108

[2] Institute of Geology, University of Innsbruck, Innrain 52, 6020 Innsbruck, Austria

[3] Department of Oceanography, Texas A & M University, College Station, TX

[4] Woods Hole Oceanographic Institution, Woods Hole, MN

[5] Department of Earth and Environmental Sciences, University of Michigan – Ann Arbor, Ann Arbor, MI, 48109

[6] Department of Bacteriology, University of Wisconsin–Madison, Madison, WI, 53706, USA

[7] School of Earth, Environmental, and Marine Sciences, University of Texas Rio Grande Valley, Edinburg, TX, 78539

* Corresponding author: toner@umn.edu

Abstract

Processes active within buoyant hydrothermal plumes are expected to modulate the flux of elements, such as Fe, to the deep ocean; however, they are yet to be described in a comprehensive manner through observations or models. In this study, we compare observed particulate Fe (pFe) speciation with thermodynamic (equilibrium) reaction path modeling for three vent fields in the Eastern Lau Spreading Center (ELSC). At each site, particles were collected from the buoyant rising portion of hydrothermal plumes using in situ filtration with a Remotely Operated Vehicle. Filter bound particles were analyzed by synchrotron micro-probe X-ray fluorescence mapping (XRF), X-ray diffraction (XRD), XRF spectroscopy, and X-ray absorption near edge structure (XANES) spectroscopy at the Fe 1s edge, as well as XRF-based chemical speciation mapping for Fe. For buoyant plumes of the ELSC, diversity in solid-state chemistry was high, and poorly crystalline, meta-stable phases were common. We demonstrate that to fully describe the crystalline-to-noncrystalline character of plume pFe, a multi-modal XRD-XANES analytical approach is needed. We found that an equilibrium modeling approach worked well for pyrite but performed poorly for important families of meta-stable pFe, namely Fe (oxyhydr)oxides and monosulfides. Based on our findings, we recommend future field expeditions strategically explore sites representing a diversity of site-specific conditions to better capture the full range of processes active in plumes. We also recommend development of kinetic models, as well as expansion of thermodynamic databases to better reflect the solid-state composition of plumes. These steps should allow oceanographers to understand the processes controlling Fe speciation in plumes well enough to create realistic models of hydrothermal fluxes to the ocean.

1. Introduction

Hydrothermal systems are globally distributed hydrologic features in which the flux of elements from the subseafloor to the base of the oceanic water column is modulated (German and Seyfried, 2014). At high temperature vents, physical, chemical, and microbiological processes active within buoyant hydrothermal plumes further regulate the gross flux of elements exiting the seafloor. Buoyant plumes are characterized by high dilution of vent fluids by entrained seawater (ca. 1:10,000), rise times of approximately one hour, and rise heights on the order of 200 m (German and Seyfried, 2014; Jiang and Breier, 2014; Speer and Helfrich, 1995). Thus far, however, these turbulent, dynamic, and heterogeneous systems have eluded a global-scale understanding of their impact on ocean biogeochemistry (e.g. (Cron et al., 2020; Estapa et al., 2015; Mottl and McConachy, 1990; Sheik et al., 2015). Based on current knowledge of neutrally buoyant plumes, it is likely that processes active within buoyant plumes will govern key aspects of element fluxes, such as Fe, to the deep ocean, as well as speciation, potential for transport, and reactivity during transport (reviews by (Gartman and Findlay, 2020; Toner et al., 2015). Recent work has demonstrated that Fe in the particulate size class (pFe; ca. > 200 nm) can be transported 100s to 1000s of kilometers off axis (Fitzsimmons et al., 2017; Hoffman et al., 2018; Lam et al., 2018; Lee et al., 2018). The analytical tools needed to measure the solid-state chemistry, or speciation, of hydrothermally derived pFe are well established (e.g. (Toner et al., 2015). However, measuring the speciation of pFe, as well as other relevant size fractions, across a sampling of sufficiently diverse vent fields to arrive at a representative cross-section of global-scale ocean inputs represents a daunting and currently intractable challenge. What we present here is an integrative approach that combines direct observations of pFe speciation with high chemical resolution with thermodynamic modeling. Our goal is to develop a framework that can

69 be used to identify critical vent-types, in different physical and geological environments
70 worldwide, where targeted field campaigns could then be used to test and validate modeling
71 approaches.

72 Thermodynamic modeling can be used to predict which minerals will be present at
73 chemical equilibrium given input concentrations of dissolved species (mixing of vent fluids with
74 deep-sea water) and known temperature and pressure conditions (Bowers and Taylor, 1985;
75 Janecky and Seyfried, 1984; McCollom, 2000). Iron-bearing minerals present at equilibrium are
76 those that draw down the activity of $Fe^{2+}_{(aq)}$ or $Fe^{3+}_{(aq)}$ to the greatest extent; these minerals are
77 defined as stable phases. Any Fe-bearing minerals known to be present in samples from the
78 field, but not predicted to be present at equilibrium, are meta-stable phases. The degree to which
79 a thermodynamic model will faithfully predict mineral phases depends first on the
80 thermodynamic database used in the model. Available thermodynamic parameters are biased
81 toward well crystalline materials with no impurities or defects. Based on the results of studies of
82 neutrally buoyant plumes (e.g. (Breier et al., 2012)), these characteristics (crystalline, no
83 impurities, no defects) may be unrepresentative of many phases precipitating in buoyant plumes.
84 Next, the quality of model predictions will depend on the degree to which equilibrium is
85 achieved. For Fe-bearing phases that rapidly precipitate as a stable phase, thermodynamic
86 modeling should provide a realistic view of pFe speciation. However, for Fe-bearing phases that
87 come to equilibrium slowly, relative to mixing and transport times, thermodynamic modeling
88 may fail to predict the actual (meta-stable) pFe phases formed in buoyant plumes.

89 Particulate Fe speciation is complex for neutrally buoyant plumes and a continuum of
90 crystalline to non-crystalline phases are observed (Breier et al., 2012; Hoffman et al., 2018;
91 Toner et al., 2009a). The gold standard of phase identification is X-ray diffraction (XRD), and

this mode of detection relies on Bragg diffraction phenomena resulting from repeating structural motifs. In other words, it relies on the well-crystalline character of solids. For poorly crystalline materials—or materials with nanometer size, impurities, or defects—XRD typically fails to produce signals that are decipherable in complex materials like hydrothermal plume particles. For poorly crystalline phases, X-ray absorption spectroscopy (XAS) can be used to accomplish phase identification by observing the valence state and local coordination environment for a specific element. Since this approach does not rely on crystallinity, it can detect poorly crystalline phases. However, XAS requires a geochemically relevant reference database for data analysis and detects just one element at a time (e.g. all Fe-bearing phases present).

Hydrothermal plumes are known to produce two major families of Fe-bearing minerals or phases, Fe sulfides and Fe (oxyhydr)oxides (oxides, hydroxides, and oxyhydroxides) (Breier et al., 2012; Campbell, 1991; Cowen et al., 1986; Feely et al., 1994; Feely et al., 1987; Gartman et al., 2019; Toner et al., 2009a; Yucel et al., 2011). While both families have exemplary crystalline members, e.g. pyrite (FeS_2) and goethite (α-FeOOH), both also contain variable stoichiometry and poorly crystalline members, e.g. pyrrhotite ($Fe_{1-x}S$; x = 0 - 0.17) and ferrihydrite ($Fe_2O_{3-0.5y}(OH)_y \cdot nH_2O$; y = 0 – 1.96; n = 0.82 – 1.14) (Yu et al., 2002). Therefore, a complete understanding of pFe in buoyant plumes requires more than one analytical approach.

In this study, we have measured pFe speciation within buoyant hydrothermal plumes and determined the degree to which pFe speciation is represented accurately by a thermodynamic modeling approach. For buoyant plumes at the Kilo Moana, ABE, and Mariner vent fields of the Eastern Lau Spreading Center (ELSC), we used synchrotron micro-probe XRD and XAS to measure the solid-state chemistry of particles retained on 0.8 µm pore-size filters. The pFe results, composed of both crystalline and poorly crystalline Fe-bearing phases, were then

compared to thermodynamic modeling results. We use the lessons learned from that comparison to propose several best-practices that should help our research community build a foundation for modeling hydrothermal Fe fluxes to the ocean in terms of field studies, analytical observations, and model development.

2. Methods and Materials

2.1 Site Description

The Lau Basin is located adjacent to the Australian-Pacific convergent plate boundary in the South Pacific Ocean. Back-arc spreading along the length of the Lau Basin is dominated by the Eastern Lau Spreading Center (ELSC) which extends ~400km, North to South, and can be sub-divided into three morphologically distinct ridge sections: the Northern and Central Eastern Lau Spreading Centers (N-ELSC, C-ELSC), and the Valu Fa Ridge (VFR) (Ferrini et al., 2008). Each section of this back-arc spreading center is characterized by differing spreading rates and host geology which vary systematically from south to north as separation from the Tonga volcanic arc increases (Martinez et al., 2006). The N-ELSC begins at 19°20′S and extends to 20°32′S with a spreading rate of 96 mm/yr. The seafloor of the N-ELSC lies at water depths of 2500-2000m and is covered uniformly by pillow lavas. The C-ELSC is defined as the area from 20°32′S to 21°26′S. It exhibits spreading rates that decrease from 75 mm/yr to 61mm/yr from North to South and the seafloor is covered by pillow and lobate lava. Axial magma chambers underlie much of the ELSC and reach a depth of 2-2.5 km below the seafloor at the central-ELSC (Jacobs et al., 2007). The southernmost segment from 21°26′S to 22°45′S, the Valu Fa Ridge, is the shallowest portion of the ELSC. Spreading rate along the VFR decreases from 61 to 31mm/yr from north to south.

During hydrothermal exploration along the ELSC under the auspices of the Ridge 2000 program, multiple hydrothermal plume anomalies were detected, six of which were then tracked to their source using the ABE autonomous underwater vehicle for follow-on detailed process studies (Ferrini et al., 2008; German et al., 2008; Martinez et al., 2006). Here we report on buoyant plume process studies conducted at three of those sites, the Kilo Moana, ABE and Mariner sites.

2.1.1 Kilo Moana Vent Field (20°3'11.52"S, 176°7'53.76"W) - Kilo Moana is located 500 m west of the northern-ELSC spreading axis on a slightly asymmetric bathymetric high (Ferrini et al., 2008). Temperatures at Kilo Moana reach up to 333 ºC at water depths of 2620 m. The Kilo Moana vent field is surrounded by basaltic substrate host rock dominated by pillow lava and little sediment cover (Bezos et al., 2009). Bathymetric maps reveal two wide volcanic domes that are cross cut by two well-defined fissures running north-south. The western fissure is 9 m deep and 4-20 m wide while the eastern fissure is 10 m deep and 5 m wide. Hydrothermal vent structures are evident adjacent to and at the intersection of both fissures. Hydrothermal activity extends north-south for ~130 m with three localized areas of high-temperature venting and diffuse flow. Kilo Moana chimneys are ~5 m tall with coalesced pipes, cactus-like protrusions, and beehive-like structures with chalcopyrite (CuFeS) and wurtzite ((Zn,Fe)S) lined conduits (Evans et al., 2017). The end member vent fluids from the Kilo Moana vent field have a pH of 3.5 and concentrations of dissolved sulfide, Fe, and Mn of 5.7, 3, and 0.6 mmol/kg seawater, respectively (Mottl et al., 2011).

2.1.2 ABE Vent Field (20°45'42.84"S, 176°11'27.6"W) - Located in the central-ELSC region, the ABE vent field is 600 m west of the spreading axis at a water depth of 2220 m and is characterized by vent fluids with temperatures up to 309 ºC. ABE is surrounded by pillow and

lobate lava host rock with moderate sediment cover and is close to a northeast-southwest oriented fault with parallel steps (Ferrini et al., 2008). At least three identifiable lava flow fronts intersect faulting regions generating conditions favorable to hydrothermal activity. ABE consists of three areas of active venting spaced ~85 m apart along the dominant fault. Similar to Kilo Moana, vent fluids create chalcopyrite and wurtzite lined conduits in small, branched chimneys (Evans et al., 2017). The end member vent fluids have a pH of 4.5 and dissolved sulfide, Fe, and Mn concentrations of 3, 0.2, and 0.3 mmol/kg seawater, respectively (Mottl et al., 2011).

2.1.3 Mariner Vent Field (22°10'48"S, 176°36'6.12"W) - Located along on the eastern limb of an overlapping spreading center on the Valu Fa Ridge section of the southern-ELSC, Mariner is the shallowest vent field at 1910 m water depth. In contrast to Kilo Moana and ABE, local faults and fissures are notably absent at Mariner. Heavy sediment cover and felsic host rock, ranging from basalt enriched with lithophile elements to andesite, surrounds Mariner (Jacobs et al., 2007). The vent field is dominated by numerous flat-topped and crater lava domes. Venting at Mariner occurs from the base and sides of 10 to 25 m tall, narrow pinnacle structures. High temperature fluids up to 363 ºC exit through chalcopyrite-lined conduits and porous beehive structures. Higher temperatures combined with the absence of faulting and abundance of magmatic carbon dioxide, suggest hydrothermal activity at the Mariner vent field is the result of magmatic rather than faulting processes (Evans et al., 2017; Mottl et al., 2011). The end member vent fluids have a pH of 2.6 and dissolved sulfide, Fe, and Mn concentrations of 6, 11, and 5.6 mmol/kg seawater, respectively (Mottl et al., 2011).

184 **2.2 Sample Collection**

185 Samples were collected on two cruises of the *R/V Thompson* to the Lau Basin (TN235 and
186 TN236) in 2009. Plume particles were collected from the buoyant plume of three vent fields
187 using the *ROV Jason II* and a suspended-particle rosette (SUPR) multi-sampler capable of
188 collecting 24 discrete samples on 0.8 µm polycarbonate membrane filters (Breier et al., 2009). A
189 hose extension was fitted to the *ROV Jason* to allow for sampling fluids within the buoyant
190 plume. Variability in particle concentration, caused by turbulence within the plume as it rises,
191 necessitated collection times from 10-30 min/sample. Sampling was conducted by: (1)
192 approaching a vent structure from the side; (2) collecting a near bottom background (NBB)
193 sample; (3) placing the sampling hose above the vent and within the buoyant plume and
194 collecting a sample; (4) *the ROV* was then piloted vertically within the buoyant plume (using the
195 ROV's auto x-y positioning capabilities) to the next requested sampling height, using the ROV's
196 altimeter to monitor height above the seafloor.

197 To preclude contamination of our samples, all sampling components were cleaned with a 5%
198 ethanol / 5% HCl (Seastar) solution. Plasticware was rinsed with MilliQ purified water and
199 leached with 10% HCl (Seastar) at pH 2. Once aboard ship, filter bound samples were recovered
200 from the SUPR sampler in an argon purged glovebox, packed in plastic vacuum containers
201 within the same argon purged glovebox, and stored and shipped frozen.

202 Near-bottom background (NBB) samples were collected at the ABE and Kilo Moana vent
203 sites near the seafloor at the outset of the plume profile prior to sampling within the rising plume
204 (Figure 1). Samples were collected in four locations at the Kilo Moana vent: two were within the
205 buoyant plume at 0.5 m and 200 m plume elevation and two were background samples, one from
206 the water column above the plume (above plume background (APB)) and one from the bottom

water near the vent (NBB). At the ABE vent site, samples were collected within the buoyant plume at 0.5 m, 10 m, 40 m, and 200 m plume elevation, as well as above plume background and near bottom background samples (Figure 1). Finally, at the Mariner vent field, two samples were collected from within the buoyant plume at 0.5 m and 25 m plume elevation.

2.3 Bulk Geochemistry

Particulate filter samples were collected with 37 mm diameter, 0.8 μm poresize polycarbonate membranes (GE Osmonics). Filter membranes were completely digested in 30 mL acid cleaned perfluoroalkoxy vials (Savillex) using the following procedure based on Bowie et al. (Bowie et al., 2010). Each filter was added to a digestion vial with 2 ml concentrated nitric acid. The vials were capped and heated at 110° C for 4 hrs. After cooling 0.5 mL of concentrated hydrofluoric acid was added to each vial. The vials were capped and heated at 110° C for 4 hrs. The vials were then uncapped and heated at 120° C to dryness. An additional 100 μL of concentrated nitric acid was added and similarly taken to dryness to facilitate evaporation of the hydrofluoric acid. After cooling, the digested sample was taken back into solution by adding 3 mL of a 3% nitric acid matrix. The vials were capped and heated for 1 hour at 60° C. This process resulted in the complete digestion of visible particles and in most cases the filter, in the few cases where residual filter material (<1% of the whole filter) remained it was removed by filtration of the digest solution. All acids were trace metal grade (Optima, Fisher Scientific). Vials were heated in a temperature-controlled hot plate (Qblock, Questron Technologies). Aliquots of sample digest, at a 1:10 dilution, were analyzed for Fe on a Varian 730-ES axial spectrometer by Activation Laboratories. External standards were used for instrument calibration. Digestion and analysis were both monitored by processing and comparing filter and

230 acid blanks, geostandards (MAG1 & BHVO), and our internal sulfide standards by these same
231 methods (Breier et al., 2012; Govindarajan, 1994).

232 **2.4 Synchrotron X-ray MicroProbe Analysis of Particles**

233 All synchrotron analyses for this project were analyzed at the Advanced Light Source,
234 Lawrence Berkeley National Laboratory, using the hard X-ray microprobe beamline (BL) 10.3.2
235 (Marcus et al., 2004). Approximately one hour prior to each analysis, a sample-bearing filter
236 was defrosted and mounted to an aluminum sample holder. During the X-ray microprobe
237 measurements, buoyant plume particles were exposed to ambient temperature and atmosphere.
238 After analysis, samples were returned to an argon filled glove box, sealed into plastic bags before
239 being heat-sealed in mylar pouches with oxygen scrubbers (Anaero Pack, Mitsubishi Gas
240 Chemical Co., Inc.) and re-frozen prior to return to the laboratory at the University of Minnesota.

241 Data collection at BL 10.3.2 for filter-bound plume particles had the following task flow:
242 (1) X-ray fluorescence (XRF) mapping at multiple energies to determine the spatial distribution
243 of elements in the particles; (2) point X-ray absorption near edge structure (XANES)
244 measurements within XRF mapped areas at the As, Fe, Mn, and V 1s (or K-edge) absorption
245 edges to define particle chemistry; (3) point X-ray diffraction (XRD) and point XRF spectra
246 were measured for particles within the XRF mapped areas; (4) Fe speciation mapping to quantify
247 the relative abundance of Fe species; and (5) additional point Fe XANES to validate the fits to
248 the speciation map.

249 **2.4.1 X-ray Fluorescence Mapping** - X-ray fluorescence mapping typically included: (1)
250 an "As map" with incident energy set to PbL3-50, or 12,985 eV, that provided Fe, Ni, Cu, Zn, and
251 As distributions; (2) a "Mn map" with incident energy set to FeK-50, or 7062 eV, that provided
252 Mn distribution without interference from Fe Kα fluorescence emission; (3) a "V map" which was

generated by subtracting a VK-50, or 5415 eV map from a VK+100, or 5565 eV to distinguish V Kα from Ti Kβ fluorescence emission; and (4) maps for Si, S, Cl, K, and Ca that were typically obtained from the lowest energy map collected (e.g. the below-V map at 5415 eV). Individual XRF maps were deadtime corrected, aligned, and channels of interest were added to a single composite map using custom beamline software (Marcus et al., 2004).

2.4.2 Point XANES - X-ray absorption near edge structure spectroscopy was conducted at the V, Mn, Fe, and As K (or 1s) absorption edges using a 7-element germanium detector in fluorescence mode. The monochromator energy calibration was set with the inflection point of a scan of V foil at 5463.76 eV, Mn foil at 6536.95 eV, and Fe foil at 7110.75 eV, or set at the white line maximum of a scan of sodium arsenate powder at 11,875 eV. The V, Mn, Fe, and As XANES spectra were collected in the range 5350-5720 eV, 6439-6838 eV, 7011-7414 eV, and 11,769-12,179 eV, respectively. Individual scans collected at the same sample location were examined for changes in line-shape and peak position, and no photon-induced sample damage was observed.

2.4.3 XANES Data Analysis - Spectra were deadtime corrected, energy calibrated, and averaged using custom beamline software (Marcus et al., 2004). The software program Athena was used to perform pre-edge subtraction and post-edge normalization (Ravel and Newville, 2005). Normalized spectra were subjected to linear combination fitting (LCF) with reference spectra using custom beamline software (Marcus et al., 2004) as described in (Breier et al., 2012). For Fe, the reference spectra database has 94 entries (Hansel et al., 2003; Marcus et al., 2008; Toner et al., 2012a). For As, the reference spectral library consists of 20 unpublished entries (Nicholas et al., 2017). For Mn, the peak positions were compared to published values for Mn(II), Mn(III), and Mn(IV) (Bargar et al., 2000). For V, the peak positions were compared to

276 published values for 19 V species (Shafer et al., 2011). The LCF results were ranked using the
277 normalized sum-squares (NSS) parameter:

278 $$NSS = 100 \times \{\sum(\mu_{exp} - \mu_{fit})^2 / \sum(\mu_{exp})^2\}$$

279 Where μ represents the normalized absorbance of the experimental (μ_{exp}) and fit (μ_{fit}). Additional
280 components were added to a fit when the change resulted in an improvement in the *NSS* by ≥
281 10%.

282 **2.4.4 X-ray Diffraction-** Microprobe XRD patterns were collected at an incident energy
283 of 17 keV (λ=0.729 angstrom) with 240-second exposure and a spot size of 6 × 11 μm. The XRD
284 patterns were radially integrated to obtain profiles of intensity versus 2θ using the freeware Fit2D
285 after calibration of sample-to-detector distance with data from an Al_2O_3 (alumina) standard
286 (Hammersley et al., 1996). Background filter XRD scans were collected.

287 Sampled XRD patterns underwent JADE software peak analysis (Materials Data Inc).
288 Background filter XRD patterns were displayed and individually subtracted from each sample
289 pattern. Additional background noise detected by JADE was subtracted to produce a uniform
290 baseline for the XRD patterns. Sampled patterns underwent peak identification using the mineral
291 standards of MDI-500 and AMCS databases to produce a list of possible standard-to-sample
292 mineral matches. The chemistry filter function in JADE was used to search for matches
293 containing elements identified by XRF spectra collected at the same location as the XRD pattern.
294 Each listed match was quantitatively assigned a Figure of Merit (FOM) number based on the
295 quality of match where an FOM number (or rating) of zero represents a perfect sample-to-
296 standard correlation and an FOM $\leq$ 25 represents an imperfect standard-to-sample match due to
297 missing, oversized, or offset peaks from pattern.

298 Analyzing XRD mineral data from natural samples poses a number of challenges and
299 standard protocols for XRD pattern identification did not work well for most of our data;
300 therefore, we developed a *best-fit* point system to rank potential matches. We assigned two
301 points to potential minerals with an assigned FOM of 25.0 or below and one point to potential
302 minerals with an assigned FOM 25.1 or above. One additional point was given to potential
303 minerals that corresponded with XRF identified elements. A maximum *best-fit* score of 3
304 represents a highly confident mineral identification (additional details on XRD data collection
305 and point system in Supporting Information).

306 **2.4.5 Chemical Mapping -** An Fe speciation mapping protocol developed for
307 hydrothermal plume particles at the East Pacific Rise (Toner et al., 2012a; Toner et al., 2015;
308 Toner et al., 2014) was applied to the ELSC samples. The method has components similar to
309 chemical/speciation/multi-energy mapping methods developed for As, (Nicholas et al., 2017), Fe
310 (Lam et al., 2018; Mayhew et al., 2011; Toner et al., 2012b), and S (Zeng et al., 2013). Briefly,
311 multiple XRF maps were collected from sample areas with energies spanning the Fe K
312 absorption edge. The number of XRF maps, and the incident energy for each, was selected based
313 on: 1) the Fe species observed in point XANES spectra; and 2) the degree to which the energies
314 distinguish among the species present. This selection process was aided by a custom beamline
315 program called *Chemical Map Error Estimator* (Nicholas et al., 2017; Zeng et al., 2013).
316 For the ELSC plume particles, point XANES indicated that 8 incident energies were
317 needed to describe the Fe species present: 7110 eV for pre-edge background, 7113.3 eV for
318 pyrite, 7120.9 eV for pyrrhotite, 7125 eV for goethite, 7133 eV for 2-line ferrihydrite, and 7350
319 eV as the post-edge map for normalization. After collecting data on roughly half of the samples
320 we identified the need to add additional energies to identify the difference between silicate and

non-silicate Fe(II). The XRF maps were deadtime corrected, registered, and compiled into a single file that is referred to hereafter as a "speciation map". All speciation maps were fit pixel-by-pixel using LCF with reference spectra and a materials blank.

The resulting speciation maps are three-dimensional datasets composed of an x-y plane representing the surface of the sample filter and a z-axis at every pixel representing an absorption profile as a function of incident energy. These absorption profiles are XANES spectra with low spectral resolution so the fit results are binned into species groups. For example, we cannot distinguish among Fe(III) oxyhydroxides with our speciation maps (e.g. goethite from akaganeite), but we can distinguish Fe-sulfides from Fe(III) oxyhydroxides (e.g. pyrite from any of the oxyhydroxides). Species bins that reflect our ability to distinguish different Fe species groups were used. Point Fe XANES data were then collected at select points within the speciation map area to ground-truth the fit.

2.6 Geochemical Reaction Path Modeling

Equilibrium thermodynamic reaction path modeling was used to predict chemical concentrations, activity coefficients, and mineral saturation states during the mixing of seawater with end member vent fluid from the A1 vent at the ABE hydrothermal field, the MA1 vent at the Mariner hydrothermal field, and the KM1 vent at the Kilo Moana hydrothermal field (Mottl et al., 2011) (Table S4). Our approach follows those of past studies (Bowers and Taylor, 1985; Janecky and Seyfried, 1984; McCollom, 2000); and, our specific plume thermodynamic model implementation has been described previously (Anantharaman et al., 2013; Anantharaman et al., 2014; Breier et al., 2012). The following is a brief description of model aspects specific to this study.

344 Vent fluid compositions (Table S4) are based on measurements made from samples
345 collected in 2005 (Mottl et al., 2011; Seewald, 2005). Vent fluid concentrations for Cu, Zn, and
346 Ba are based on EPR 21° N for lack of more relevant data (Von Damm et al., 1985). In situ pH
347 was calculated from measurements of pH at 25° C using an equilibrium reaction path model that
348 increased the temperature of the measured fluid to the original vent fluid temperature.
349 Background seawater dissolved O_2 concentrations are based on WOCE measurements from
350 section P06 (Talley, 2007). Background seawater dissolved H_2 is assumed to be controlled by
351 atmospheric equilibrium; this is consistent with previous findings for H_2 in the Atlantic Ocean
352 (Conrad and Seiler, 1988). Note, the available vent chemistry and background seawater
353 chemistry data predates this study; actual chemistries for these parameters may have differed
354 during this study.
355 Reaction path modeling was performed with REACT, part of the Geochemist's
356 Workbench package. The plume reaction path is modeled through a mixing process that ends at a
357 vent fluid to seawater dilution of 1 part in 10,000, encompassing dilutions across the full rise-
358 height of a buoyant hydrothermal plume. Precipitated minerals were allowed to dissolve and
359 their constituents to re-precipitate based on thermodynamic equilibrium constraints. The
360 thermodynamic data upon which this model is based was predicted by SUPCRT95 (Johnson et
361 al., 1992) for the temperature range of 1-425° C (specifically 1, 25, 60, 100, 225, 290, 350, and
362 425° C) and a pressure of 500 bar, a pressure and temperature range that encompasses all known
363 deep sea vents. SUPCRT95 uses previously published thermodynamic data for minerals, gases,
364 and aqueous species (Helgeson, 1978; McCollom and Shock, 1997; Saccocia and Seyfried, 1994;
365 Shock and Helgeson, 1990; Shock et al., 1989; Shock et al., 1997; Sverjensky et al., 1997).
366 Thermodynamic data for pyrolusite, bixbyite, hausmannite, and marcasite were added from

Robie et al. (Robie, 1979) and thermodynamic data for $Fe(OH)_3$ were added from Wagman et al. (Wagman, 1982). Additional H_2-producing reactions for the formation of elemental S, bornite, pyrite, chalcopyrite, and covellite were also added (McCollom, 2000). The B-dot activity model was used (Helgeson, 1969; Helgeson, 1974). Temperature dependent activity coefficients were used for aqueous CO_2 and water in a NaCl solution (Bethke, 2007; Cleverley and Bastrakov, 2005; Drummond, 1981). A general limitation of REACT is that it does not predict the thermodynamic behavior of solid solutions. Thus minerals such as sphalerite, pyrrhotite, chalcopyrite, and isocubanite are treated as separate phases with ideal stoichiometry. This may influence the predicted plume mineral

Following assumptions used in previous models, HS^-/SO_4^{2-} equilibration was suppressed on the basis that this reaction is kinetically inhibited on the short timescales of transport in the rising plume. For similar reasons, the precipitation of quartz and other silicate minerals were also suppressed in previous studies. Here, however, we consider the potential precipitation of trace and non-equilibrium minerals as well as equilibrium minerals. For this reason, all minerals were allowed to precipitate when thermodynamically predicted to do so. The ratio of the ion activity product and the thermodynamic solubility product were predicted for all minerals in the model so that the saturation state of trace and minor minerals could be evaluated. Precipitated minerals were allowed to dissolve and their constituents to re-precipitate based on thermodynamic equilibrium constraints. Consequently, a summation of minerals present at any point in the reaction path would only represent a subset of all minerals that precipitate during the process; these values can be mutually exclusive (e.g., pyrite, magnetite, and Fe hydroxide) and should not be integrated along the reaction path. To summarize all of the minerals that precipitate during the reaction path, Table S5 lists the set of minerals that achieve a saturation index of 1 and achieve

390 an equilibrium state along the modeled reaction path (Supporting Information). In addition,
391 Table S5 also lists those minerals that achieve lower saturation indices because they have the
392 potential to precipitate if plume physical or chemical conditions are different or where kinetic
393 inhibitions prevent other minerals from precipitating.
394
395 # 3. Results
396 Particle chemistry (> 0.8 μm) in buoyant plumes along the ELSC was investigated at the
397 Mariner, ABE, and Kilo Moana vent fields. Buoyant plume samples from each location were
398 collected by *in situ* filtration and bulk major element concentration was measured by digestion
399 and ICP-MS. Figure 1 shows a schematic of the ABE plume indicating elevations above the
400 vent where samples were collected and approximate location of near bottom background (NBB)
401 and above plume background (APB) samples. Mariner and Kilo Moana vent fields were
402 sampled in a similar way. Total particulate iron concentrations ranged from < 4 nmol Fe/kg
403 seawater in above plume background (APB) samples to 204 nmol Fe/kg at a plume elevation of
404 0.5 m at Mariner (Table 1). Within the ABE plume, particulate Fe concentrations decreased
405 from 19 nmol Fe/kg near the source of the plume (1.5 m) to 4 nmol Fe/kg at a plume elevation of
406 200 m above the vent (Table 1).
407
408 ## 3.1 Particulate Fe Chemical Speciation
409 In this study, we measure pFe specation using two different synchrotron X-ray
410 microprobe approaches, point XANES and chemical mapping, that rely on X-ray absorption
411 phenomena (Toner et al., 2015; Toner et al., 2014; Toner et al., 2012b). In practice, these two
412 approaches are applied iteratively with the findings of one observation type informing data

413 collection and analysis in the other (Nicholas et al., 2017). The point XANES data, in
414 conjunction with multi-element XRF mapping, are used to generate a complete list of Fe species
415 present in the filter-bound sample. Points for XANES analysis are chosen to query Fe in
416 different chemical environments according to co-located elements (identified from XRF maps)
417 or different Fe species (identified by chemical maps). This means that the points are not selected
418 at random to quantify the distribution of Fe species on the filter. Rather, the goal was to discover
419 the number of different types of Fe species present in the sample and collect high quality spectra
420 for phase identification of those types. The chemical mapping approach trades spectral, and
421 therefore chemical, resolution for a larger number of observations. The strength of the chemical
422 mapping is that the true quantities of Fe species present can be measured for a filter-bound
423 sample. Using these two complementary approaches together, a typical experiment for a filter-
424 bound sample could include tens of point XANES with high spectral resolution, and a chemical
425 map with 100,000+ observations (i.e. pixels) with low spectral resolution. The purpose of
426 pairing point XANES observations (high spectral resolution) with chemical mapping (low
427 spectral resolution but large number of points queried) is to overcome the quantification issue
428 caused by non-random selection of XANES points. If the number of XANES points is
429 increased, then the Fe speciation measured by XANES will converge with that observed with
430 chemical mapping. Similarly, if the number of incident energies in a chemical map is increased,
431 then the specificity of the Fe species bins, and the overall quality of phase identification, will
432 converge with the level of detail obtained by point XANES.

433 Point Fe XANES were collected and analyzed for solid particulate samples from buoyant
434 plumes at the ABE, Kilo Moana, and Mariner vent-fields. Linear combination fitting results
435 from spectra were pooled and binned to produce a data set with 6 different Fe speciation

436 categories: Fe(0), Fe-sulfide, Fe-silicate, Fe(II), Fe(II/III), and Fe(III), and their *estimated*
437 relative proportion within a given sample. Iron speciation mapping was used for the same filter-
438 bound samples to provide an actual *measured* relative proportion of three Fe species (Fe(II),
439 Fe(III), and Fe-sulfide; additional details in Methods).

440 **3.1.1 Comparison Across Sites at 0.5 m and 200 m -** Results from point Fe XANES are
441 presented in Figure 2 for the Mariner, Kilo Moana, and ABE plumes at 1.5 m and for the Kilo
442 Moana and ABE plumes at 200 m plume elevation. Near vent, Fe in all three plumes is
443 predominately in the form of Fe-sulfide. Kilo Moana has the highest sulfide proportion at > 80
444 mol % (per atom basis), while the proportion at both Mariner and ABE lies closer to 50 % (per
445 atom basis). Mariner is the only location with a significant proportion of Fe-silicates, while the
446 ABE plume is the only one of the three with a significant pool of non-sulfide Fe(II) near vent.
447 Finally Kilo Moana is the sole plume with a sizeable proportion of Fe(II/III) mixed valence
448 minerals. Both the Mariner and ABE plumes at near vent elevation have an Fe(III) proportion of
449 15-20 %, while interestingly there is no measurable Fe(III) at 0.5 m plume elevation at the Kilo
450 Moana location (Figure 2, Table 1).

451 Moving away from the source of the plume to an elevation of 200 m, the relative
452 proportions of pFe shift in both the Kilo Moana and ABE buoyant plumes. The Fe-sulfide
453 component decreases from greater than 50 % of the total Fe to 25 % and 35 % in the Kilo Moana
454 and ABE plumes, respectively (all % per atom basis). This coincides with an increase in the
455 silicate and Fe(III) fractions in the Kilo Moana plume and a sizeable increase in Fe(III) minerals,
456 from 15 % to > 50 % (per atom basis), in the ABE plume (Figure 2).

457 Similarly, results from Fe speciation chemical mapping (Figures S2-4) indicate an
458 increase in the proportion of Fe(III) and a decrease in the proportion of reduced Fe (Fe(II) and/or

459 Fe-sulfide) between near vent and a plume height of 200 m for both the Kilo Moana and ABE
460 plumes (Table 1). For example, in the ABE plume the Fe(III) proportion increases from 33 to
461 39% while the Fe(II) concentration decreases by 50 % from 14 to 7 % and the Fe-sulfide
462 proportion remains roughly consistent at 52 - 54 % (per atom basis). The speciation differs
463 slightly in the Kilo Moana plume where the Fe(III) proportion increases from 54 to 74 % while
464 the Fe(II) contribution remains at ~10 % and the Fe-sulfide fraction decreases from 35 to 15 %
465 (per atom basis). The Mariner plume behaves differently in that as plume elevation increases the
466 proportion of reduced Fe species actually increases while the proportion of oxidized Fe
467 decreases.

468 **3.1.2 ABE Plume Profile -** Individual Fe XANES spectra for the entire ABE plume
469 profile are presented in Figure 3, allowing for a visual comparison of the presence of various Fe
470 chemical speciation types as a function of plume elevation. Spectra for known standards of an
471 Fe-sulfide (pyrite), Fe(II) ($FeCl_2$), and Fe(III) (ferrihyrdrite) are included for comparison. All
472 three Fe species are present in the near bottom background and 1.5 m samples. As plume
473 elevation increases the proportion of Fe(II) in the samples decreases; in fact, by the time an
474 elevation of 200 m is reached only Fe(III) and Fe-sulfide remain. This is generally consistent
475 with the Fe chemical speciation mapping results for the ABE profile (Table 1) where the
476 proportion of Fe-sulfide remains > 35 % at 3 out of 4 heights (all but 10 m), while Fe(III) varies
477 between 33 and 78 % depending on height and Fe(II) drops by 50 % from 14 to 7 % as height
478 increases from 0.5 to 200 m (all % on per atom basis).

479 **3.1.3 Comparison of near bottom background and above plume background -** Above
480 plume background samples were collected at 300 m above the ABE and Kilo Moana vent sites
481 and near bottom background samples were collected adjacent to the vent but out of the direct line

482 of the buoyant plume for each. Fe point XANES indicate that near bottom background samples
483 at both sites contain a combination of oxidized and reduced species with appreciable pools of Fe-
484 sulfide, Fe(II), and Fe(III) (Table 1). The ABE sample is dominated by Fe-silicates and Fe(II)
485 which each comprise 34% of the total Fe. The Kilo Moana sample has a greater amount of Fe-
486 sulfide (30% vs. 14%), 24% mixed valence Fe(II/III) phases, and no Fe-silicates. As elevation
487 increases to the above plume background sample in the ABE profile the Fe-sulfide proportion
488 increases from 14 to 20% while the Fe-silicate proportion decreases from 34 to 15%. The above
489 plume background sample is dominated by Fe(III) with 65% of the total Fe (Table 1).
490 Iron speciation chemical mapping indicates that the near bottom background sample at
491 both locations is dominated by Fe(III) species with appreciable levels of Fe-sulfide and very little
492 (< 10 %) Fe(II). The iron (III) proportion is higher at the Kilo Moana site, where it comprises 71
493 % of the Fe pool, compared to the ABE vent (52%). The above plume background samples from
494 the Kilo Moana location have appreciable proportions of all 3 Fe pools at 15%, 33%, and 52 %
495 for Fe-sulfide, Fe(II) and Fe(III), respectively. In contrast the area above the ABE plume is
496 dominated by Fe(III) at 91 %.
497 We note that there are some discrepancies between the reported values for proportions of
498 the various Fe species between the point XANES data (Figure 2) and the chemical mapping
499 results (Table 1). This is to be expected and is due to both the differing analytical methods
500 applied, as described above, and the operational realities associated with synchrotron microprobe
501 analysis of naturally heterogeneous environmental samples. A larger investment of instrument
502 time in these measurements--more XANES points, and more chemical map energies--would
503 bring the two methods into full agreement for our high heterogeneity samples. At present, the
504 complementary use of the point XANES and chemical mapping allow us to measure pFe

505 speciation in detail, including rare species, as well as calculate relative abundances of those
506 species.
507
508 **3.2 Particulate V, Mn, and As Oxidation State**
509 Vanandium, As, and Mn point XANES spectra were collected for filter-bound particles
510 within the ABE plume at 1.5 m and 200 m above the vent orifice (Figure S4). Vanadium remains
511 consistent as V(V) at both plume heights suggesting seawater is the primary source because V is
512 primarily present as vanadate in seawater (Cutter, 2001). For Mn, both Mn(II) and Mn(IV)
513 appear at 0.5 m while by 200 m all Mn appears to have been oxidized to Mn(IV). Similar
514 oxidation occurs between 0.5 m and 200 m for As where measured oxidation state changes from
515 As(III) to As(V) (Figure S1).
516
517 **3.3 Mineralogy of Crystalline Phases**
518 Synchrotron microprobe X-ray diffraction (XRD) patterns were collected and analyzed
519 using JADE peak analysis software. Fits of Merit (FOM) and elemental composition (XRF
520 spectroscopy) was used to devise a best fit scoring system where minerals that scored a best-fit
521 of 3 were considered as detected (details in Supporting Information). X-ray diffraction is most
522 effective at detecting crystalline phases in our system. Phases detected by XRD on the filter-
523 bound particles are presented in Table 2 (with phase names and idealized formulas); a subset of
524 these phases was also detected by Fe XANES (Table 2 and Figure 4). Figure 4 shows the
525 method(s) that yielded positive detection for all Fe-bearing minerals predicted by geochemical
526 modeling. From a total of 10 Fe-bearing phases included in the model, three were detected by
527 XRD only, three more (hematite, pyrrhotite, and pyrite) were detected by XRD and Fe XANES,

528 and the remaining 2, wurtzite and chalcopyrite, were only detected by XRD. Both pyrrhotite and
529 wurtzite were detected by XRD at 2 out of 3 vent sites, while pyrite was the only Fe-bearing
530 mineral detected by XRD at all 3 sites. The ABE vent site had the most XRD detected Fe
531 minerals with 4 while Mariner and Kilo Moana had only 3 and 2 respectively (Figure 4).

532 The number of minerals phases detectable by XRD in our systems is greater for Fe-sulfur
533 compounds than for Fe (oxyhydr)oxides. For example, only one Fe (oxyhydr)oxide, hematite, is
534 detected by XRD while 5 individual Fe-S phases: pyrite, chalcopyrite, wurtzite, are all detected
535 by XRD (Table 2). This is attributed to diffraction detecting only the more crystalline materials
536 in our system. Additionally, a considerable number of metal sulfides (metals other than Fe),
537 sulfates, halides, and phosphates that are detected by XRD. While various metal sulfides are
538 detected at all 3 vent sites, the vast majority of sulfate, halide, and phosphates are detected at the
539 Mariner site (Table 2).
540

541 **3.4 Mineral Precipitation Predicted by Reaction Path Modeling**

542 Thermodynamic reaction path modeling was performed with REACT, part of the
543 Geochemist's Workbench package. Predictions for the mineral precipitation resulting from the
544 convective mixing of 1 kg of each of ABE, Kilo Moana or Mariner vent fluid with surrounding
545 seawater to plume dilutions of 1:10,000 and a final mixture temperature of 2°C are presented in
546 Figure S5. Quartz, dolomite, dolomite-ordered, and pyrolusite precipitation paths are predicted
547 but are likely kinetically limited in this environment; formation of other minerals may also be
548 kinetically limited to varying degrees. Several minerals are predicted to precipitate over a wide
549 range of temperatures at all three sites including pyrite and hematite. For example, pyrite is
550 predicted to form from 309°C to approximately 30°C in concentrations ranging from a maximum

551 of 30 mg kg^{-1} vent fluid in the ABE reaction pathway to 200 mg kg^{-1} vent fluid in Kilo Moana
552 and Mariner pathways. While the rapid pace of hydrothermal plume mixing in this system may
553 favor precipitation of amorphous mineral phases like ferrihydrite, crystalline phases such as
554 hematite are more prevalent in thermodynamic databases (Breier et al., 2012). Magnetite is only
555 predicted as an equilibrium phase at the very start of the ABE reaction path at a temperature of
556 309° C and a concentration of 1.2 mg kg^{-1} vent fluid.
557

558 # 4. Discussion

559 Hydrothermal plumes are globally distributed features in which the flux of elements from
560 the subseafloor to the base of the oceanic water column is modulated. For buoyant plumes, the
561 site-specific conditions and processes—physical, chemical, and biological—affecting the flux of
562 elements to the deep ocean are yet to be described in a comprehensive manner through either
563 observation or modeling. For elements such as Fe, processes occurring within plumes should
564 determine the overall flux of Fe to the deep ocean, as well as its potential for transport and
565 reactivity during transport. Ultimately, oceanographers seek to understand the processes
566 controlling Fe speciation in plumes well enough to create realistic models of hydrothermal fluxes
567 to the ocean. Therefore, in this study, we have sought to measure all forms of pFe speciation
568 within buoyant plumes and clarify the degree to which pFe speciation is well-represented by a
569 thermodynamic (equilibrium) modeling approach.
570

571 ## 4.1 Iron phases in thermodynamic equilibrium in the buoyant plume

572 Thermodynamic modeling predicts that the mineral magnetite (see Table 2 for phase
573 names and formulas) should form under equilibrium conditions in the ABE buoyant plume, but

574 not in the Kilo Moana or Mariner plumes. Magnetite was in fact detected with Fe XANES a
575 total of three times in our buoyant plume sample set, twice at ABE and once at Kilo Moana. One
576 observation at the ABE site was in the 200 m plume sample where 58 % of the pFe in the grain
577 examined was magnetite with the remaining Fe best represented by an Fe-substituted brucite and
578 a phyllosilicate nontronite from our reference database. A second magnetite observation in the
579 ABE plume occurred at 40 m plume elevation. In that case, 28 % of pFe was in the form of
580 magnetite while the remaining Fe was best represented by Fe in the form of augite (pyroxene)
581 and perovskite (Fe substituted Ti oxide). Magnetite was also detected in the 0.5 m Kilo Moana
582 sample where the pFe was 19 % magnetite with the remaining Fe best represented by pyrite and
583 pyrrhotite.

584 Hematite is predicted to form in buoyant plumes at all sites investigated: ABE, Kilo
585 Moana, and Mariner. However, hematite was detected just once in a single sample from the
586 ABE site at 1.5 m plume elevation. The observation was confirmed by both Fe XANES and
587 XRD analysis. In the best-fit to the Fe XANES data, hematite accounted for 89 % of pFe in a
588 grain that also contained, or was co-located with, phases most consistent with haxonite (native
589 Fe) and almandine (garnet).

590 Overall, these observations are robust in that both magnetite and hematite have unique
591 spectral signatures and the percent attributed to each of them in the best-fits is well above
592 conservative detection limits. While thermodynamic modeling indicates that magnetite (at ABE)
593 and hematite (all three sites) are stable phases at equilibrium within the plume, their presence
594 does not prove that the phases formed within the plume. Whether they formed in the plume or
595 were entrained from non-hydrothermal sources, high stability Fe oxides, magnetite and hematite,

596 account for only a very small proportion (< 2 %) of the total pFe in the ELSC samples compared
597 to the abundant metastable Fe (oxyhydr)oxides (see section 4.2).
598 Thermodynamic modeling predicts that pyrite should form at equilibrium in all three
599 buoyant plumes. Indeed pyrite was detected by both Fe XANES and XRD at every site and at all
600 plume elevations, including the background samples. Pyrite is an abundant form of Fe at the
601 ELSC and represents ~ 19 % of all pFe as measured by Fe XANES. Pyrite has a distinctive
602 spectral shape in Fe XANES spectra and is one of the few Fe-bearing minerals for which
603 inclusion in the best-fit is diagnostic for the presence of the mineral. All evidence available
604 suggests pyrite forms in the plume, reaches equilibrium quickly, and is well represented by
605 equilibrium modeling.
606 In contrast to pyrite, the sulfide mineral chalcopyrite shows poor agreement between
607 modeling and measured observations. Chalcopyrite is predicted to form at equilibrium at both
608 ABE and Kilo Moana, but was not detected by XRD at either site (the Fe XANES database does
609 not contain a chalcopyrite reference). While chalcopyrite is not predicted to form at the Mariner
610 site, it was detected with high confidence for five grains via XRD.
611
612 **4.2 Iron phases out of thermodynamic equilibrium in the buoyant plume**
613 Iron (oxyhydr)oxides are abundant and ubiquitous in the ELSC buoyant plumes and were
614 detected at ABE, Kilo Moana, and Mariner by Fe XANES spectroscopy. Across samples from
615 all three sites, the Fe(III) oxyhydroxides ferrihydrite and goethite account for ~ 17 % of the pFe
616 as detected by XANES. While Fe XANES lacks the chemical sensitivity needed to
617 unambiguously distinguish closely related Fe (oxyhydr)oxide phases, several types of Fe
618 (oxyhydr)oxides and related phases were selected as best-fits from the reference library

619 indicating diversity in the phases present. Iron oxides, hydroxides, and oxyhydroxides account
620 for ~ 34 % of the pFe measured across all sites. As a family of phases, Fe (oxyhydr)oxides
621 exhibit poor crystallinity and other characteristics that make them difficult to detect or
622 undetectable by XRD. In accordance with this only two Fe (oxyhydr)oxide phases were detected
623 in buoyant plume samples using XRD in this study (one hematite grain at ABE, one franklinite
624 grain at Mariner).

625 Overall, thermodynamic modelling and direct observations yield different views of the
626 buoyant plume for Fe (oxyhydr)oxide phases. While the thermodynamic model includes an
627 Fe(III) hydroxide representative, goethite, ferrihydrite, green rusts, and other phases that were
628 ultimately observed using Fe XANES are not included in the database. In all three ELSC
629 buoyant plumes, Fe(III) hydroxide was not predicted to be present at equilibrium (saturation
630 index = - 2).

631 There are several practical issues to consider when applying an equilibrium modeling
632 approach to Fe (oxyhydr)oxides in plumes. First, the young buoyant plume is a dynamic system
633 and is expected to be out of equilibrium for at least some phases. Second, the diversity of phases
634 present in the buoyant plume are not easily included in the model as representative
635 thermodynamic parameters are lacking. Third, even if the Fe(III) hydroxide is a reasonable
636 proxy for the family of Fe(III) (oxyhydr)oxides observed in our system, the equilibrium approach
637 will, by definition, select the single stable phase among those included in the model database.
638 For example, the Fe oxide hematite is included in the model, it has the lowest solubility and will
639 draw down the Fe^{3+}_{aq} activity to the lowest value; it is predicted, therefore, to be the stable phase
640 at equilibrium at the expense of meta-stable Fe(III) hydroxide.

While pyrrhotite was detected by Fe XANES in all three plumes, it was not predicted by thermodynamic modeling. Similar to the Fe(III) (oxyhydr)oxide phases, pyrrhotite is a family of phases and is not well distinguished from other related Fe monosulfide phases with Fe XANES. Therefore, pyrrhotite, FeS, mackinawite, troilite, pentlandite, and cubanite proportions resulting from the linear combination fits to Fe XANES spectra, are binned together in this discussion. Note that of these Fe monosulfide phases, only pyrrhotite is included in the model database. The Fe monosulfide phases account for ~ 14 % of the pFe observed across the three vent sites, and are out of thermodynamic equilibrium in all plumes (i.e. meta-stable).

4.3 Implications for modeling hydrothermal contributions of iron to the ocean

Through the study of buoyant hydrothermal plumes at three vent sites along the Eastern Lau Spreading Center, we have determined that certain pFe species are well described by an equilibrium model (e.g. pyrite), while others are not (e.g. phases within the Fe monosulfide and Fe (oxyhydr)oxide families). Here, we use the lessons learned from this study to propose several best-practices that should help our research community build a foundation for modeling hydrothermal Fe fluxes to the ocean. Our recommendations for future work span: (1) field studies; (2) analytical observations; and (3) model development.

Quantifying hydrothermal fluxes to the deep ocean, as well as long range transport potential and bioavailability, will require additional field expeditions to hydrothermal vent systems that focus on a mass balance approach to key elements in the dissolved and solid (e.g. colloidal and particulate size classes) phases. Elemental budgets at different locations within the plume system—buoyant, near-field neutrally buoyant, and far-field neutrally buoyant—should improve our understanding of net fluxes at threshold length scales from vents. The international

664 GEOTRACES program has recently revealed that submarine hydrothermal venting can, indeed,
665 impact global-scale ocean biogeochemistry over 100-1000 km length scales in every ocean basin
666 (German et al., 2016). Detailed work across GEOTRACES sections has also revealed, however,
667 that processes critical to setting the flux from hydrothermal venting to the ocean occurs on
668 shorter length scales (0-100 km) that are beyond the resolution of GEOTRACES sections
669 (Fitzsimmons et al., 2017). In addition to mass balance, concentrations of elements within
670 specific size-classes (e.g. soluble, colloidal, and particulate; e.g. ((Fitzsimmons and Boyle,
671 2014)) should be routinely measured, as well as chemical speciation (Toner et al., 2015) and
672 isotopic composition (Fitzsimmons et al., 2017) of key elements within each size-class.
673 Together, these observations will describe transport potential, relevant reactions and processes,
674 and bioavailability. While our knowledge of the range of possible processes affecting
675 hydrothermal fluxes, particularly of Fe, has increased in the past 15 years (Bennett et al., 2008;
676 Cron et al., 2020; Fitzsimmons et al., 2017; Gartman and Findlay, 2020; Hoffman et al., 2018; Li
677 et al., 2014; Lough et al., 2019; Sander and Koschinsky, 2011; Sander et al., 2007; Toner et al.,
678 2009a; Yucel et al., 2011), our understanding of which processes are important under different
679 venting scenarios is nascent. Future field expeditions should therefore aim to explore sites
680 representing a diversity of site-specific conditions to better capture the full range of processes
681 active in plumes that modulate fluxes.

682 Given the overall importance of precipitation-dissolution, aggregation, and sorption
683 reactions in hydrothermal plumes, particularly for elements such as Fe, we focus our attention
684 here on analytical recommendations for solid-state chemistry. The complexity and heterogeneity
685 of hydrothermal plume solid-state chemistry has been demonstrated using a variety of analytical
686 approaches (Breier et al., 2012; Feely et al., 1990; Findlay et al., 2019; Gartman et al., 2019;

687 Gartman et al., 2014; Klevenz et al., 2011; Toner et al., 2009b). To date, the most comprehensive
688 view of plume solid-state chemistry (organic, inorganic, crystalline, noncrystalline, and multiple
689 elements) has been gained using a suite of X-ray microscopy and microprobe tools with X-ray
690 diffraction and absorption spectroscopy detection modes (as reviewed by (Toner et al., 2015)).
691 While the number of vents investigated to date is low, measurements show that hydrothermal
692 solids in the particulate size fraction are composed of inorganic and organic phases, including
693 biota and biotic fragments, with inorganic components spanning a wide continuum of poorly
694 ordered to well crystalline phases (e.g. (Breier et al., 2012; Cron et al., 2020; Fitzsimmons et al.,
695 2017; Hoffman et al., 2018; Toner et al., 2009a; Toner et al., 2012b)). For the three ELSC vents
696 examined here, we demonstrate the necessity of measuring pFe chemistry with analytical tools
697 that capture both crystalline (XRD) and poorly crystalline (XANES) phases. The primary pFe
698 phase detected by XRD is pyrite which accounts for ~ 19 % of the Fe in the samples (per atom
699 basis). In contrast, the most abundant type of pFe observed, the meta-stable Fe (oxyhydr)oxide
700 phases, are undetectable with XRD. This is significant given that the Fe (oxyhydr)oxide phases
701 (not counting hematite and magnetite) account for ~ 33 % of the pFe (per atom basis). Similarly,
702 the Fe monosulfide phases are poorly detected by XRD and account for ~ 14 % of the Fe present
703 on a per atom basis. A suite of analytical approaches that can detect Fe phases with differing
704 amounts of crystallinity is critical to gaining a complete picture of the solid-state chemistry of
705 plume particles.

706 Here we have used a reaction path thermodynamic modeling approach that allows
707 hydrothermal vent fluids to come to equilibrium under different dilution and temperature
708 conditions, mimicking a rapidly cooling and diluting plume. Our findings, from this study and
709 others (Breier et al., 2012), reveal important mismatches between measured observations and

710 model calculations and demonstrate that disequilibrium is strong within buoyant plumes for
711 certain pFe phases. The main solid phases in the particulate size-class that are not accounted for
712 in equilibrium modeling are also the phases that are not detectable by X-ray and electron
713 diffraction analysis. The Fe (oxyhydr)oxide and Fe monosulfide families of phases are important
714 components of the pFe pool that are at present poorly represented by any equilibrium modeling
715 approach. The development of kinetic models and expansion of solid phases included in
716 thermodynamic databases is expected to provide a path forward in this key area of research.
717

718 ## Acknowledgments

719 We thank Chief Scientists Charles Fisher, Anna-Louise Reysenbach, George Luther, and
720 Peter Girgus, the *ROV Jason II* team (dives J2-421 to J2-430, and J2-434 to J2-443), and the
721 crews of the *R/V Thompson* (cruises TN235 and TN236). The research was supported by funds
722 from the National Science Foundation's Ridge 2000 program (BMT OCE-1037991; JAB OCE-
723 1038055; GJD OCE-1038006; OCE-1851007). We thank Katrina Edwards and Sheri White for
724 fieldwork support. We thank Matthew Marcus and Sirine Fakra for synchrotron support at the
725 Advanced Light Source (BL 10.3.2 and 5.3.2), as well as Sarah Nicholas, Brandi Cron
726 Kammermans, and Teng Zeng for assistance in synchrotron data collection. The Advanced Light
727 Source is supported by the Director, Office of Science, Office of Basic Energy Sciences, of the
728 U.S. Department of Energy under Contract No. DE-AC02-05CH11231. We acknowledge and
729 honor the indigenous communities native to the Twin Cities, Minnesota region where the
730 University of Minnesota now resides on the ancestral land of the Wahpekute (Dakota),
731 Anishinabewaki, and Očeti Šakówiŋ (Sioux) peoples. We wish to recognize the people of the
732 Sioux tribe as the ongoing caretakers of this land.

Table Captions

Table 1. Proportion of Fe-Sulfide, Fe(II) and Fe(III) for all sampling locations and plume elevations based on chemical mapping measurements.

Table 2. Results from X-ray diffraction (XRD) and Fe X-ray absorption near edge structure (XANES) spectroscopy detection at all three vent sites. Minerals underlined are predicted to form by geochemical modeling (saturation index, SI = 1).

Figure Captions

Figure 1. Schematic of buoyant hydrothermal plume showing plume elevation (in meters) and approximate location of sampling at ABE vent field, including the near bottom background (NBB) and above plume background (APB).

Figure 2. Results from point X-ray absorption near edge structure (XANES) spectra showing difference in particulate Fe speciation among locations, the Kilo Moana, ABE, and Mariner vent fields, for a given plume elevation. A) 0.5 m and B) 200m above the vent and within the buoyant plume.

Figure 3. Iron point X-ray absorption near edge structure (XANES) spectra showing differences in particulate Fe speciation for samples collected as the above plume background (APB), within the buoyant plume at different elevations above the vent, and a near bottom background (NBB) for the A1 vent at ABE vent field. Green and orange dotted lines represent the position of Fe(II) and Fe(III) spectra, respectively.

Figure 4. Bubble plot showing the detection mode (by color) and thermodynamic model saturation index (SI, by circle size) for Fe-bearing minerals included in the thermodynamic database according to vent field. Detection modes are: (1) not detected, ND, in grey; (2) X-ray diffraction, XRD, in red; (3) X-ray absorption near edge structure, XANES, spectroscopy, in green; and (4) both XRD and XANES in blue. The saturation index (SI) is represented by: (1) largest circles have an SI = 1, and are predicted to form in the plume by the model; and (2) smaller circles have an SI of -1 or -2 and are not predicted to form in the plume by the model.

References

Anantharaman, K., Breier, J.A., Sheik, C.S. and Dick, G.J. (2013) Evidence for hydrogen oxidation and metabolic plasticity in widespread deep-sea sulfur-oxidizing bacteria. Proceedings of the National Academy of Sciences of the United States of America 110, 330-335.

Anantharaman, K., Duhaime, M.B., Breier, J.A., Wendt, K., Toner, B.M. and Dick, G.J. (2014) Sulfur oxidation genes in diverse deep-sea viruses. Science 344, 757-760

Bargar, J.R., Tebo, B.M. and Villinski, J.E. (2000) In situ characterization of Mn(II) oxidation by spores of the marine *Bacillus* sp. strain SG-1. Geochim. Cosmochim. Acta 64, 2775-2778.

Bennett, S.A., Achterberg, E.P., Connelly, D.P., Statham, P.J., Fones, G.R. and German, C.R. (2008) The distribution and stabilisation of dissolved Fe in deep-sea hydrothermal plumes. Earth Planet. Sci. Lett. 270, 157-167.

Bethke, C.M. (2007) Geochemical and biogeochemical reaction modeling. Cambridge University Press, Cambridge, UK.

Bezos, A., Escrig, S., Langmuir, C.H., Michael, P.J. and Asimow, P.D. (2009) Origins of chemical diversity of back-arc basin basalts: A segment-scale study of the Eastern Lau Spreading Center. Journal of Geophysical Research-Solid Earth 114.

Bowers, T.S. and Taylor, H.P. (1985) An integrated chemical and stable-isotope model of the origin of midocean ridge hot-spring systems. Journal of Geophysical Research-Solid Earth and Planets 90, 2583-2606.

Bowie, A.R., Townsend, A.T., Lannuzel, D., Remenyi, T.A. and van der Merwe, P. (2010) Modern sampling and analytical methods for the determination of trace elements in marine particulate material using magnetic sector inductively coupled plasma-mass spectrometry. Anal Chim Acta 676, 15-27.

Breier, J.A., Rauch, C.G., McCartney, K., Toner, B.M., Fakra, S.C., White, S.N. and German, C.R. (2009) A suspended-particle rosette multi-sampler for discrete biogeochemical sampling in low-particle-density waters. Deep-Sea Research Part I-Oceanographic Research Papers 56, 1579-1589.

Breier, J.A., Toner, B.M., Fakra, S.C., Marcus, M.A., White, S.N., Thurnherr, A.M. and German, C.R. (2012) Sulfur, sulfides, oxides and organic matter aggregated in submarine hydrothermal plumes at 9° 50' N East Pacific Rise. Geochim Cosmochim Acta 88, 216-236.

Campbell, A.C. (1991) Mineralogy and chemistry of marine particles by synchrotron X-ray spectroscopy, Mossbauer spectroscopy, and plasma-mass spectrometry, in: Hurd, D.C., Spencer, D.W. (Eds.), Marine particles: Analysis and characterization. American Geophysical Union, Washington D.C., pp. 375-390.

807 Cleverley, J.S. and Bastrakov, E.N. (2005) K2GWB: Utility for generating thermodynamic data
808 files for The Geochemist's Workbench® at 0–1000°C and 1–5000bar from UT2K and the
809 UNITHERM database. Computers & Geosciences 31, 756-767.
810
811 Conrad, R. and Seiler, W. (1988) Methane and hydrogen in seawater (Atlantic Ocean). Deep Sea
812 Research Part A. Oceanographic Research Papers 35, 1903-1917.
813
814 Cowen, J.P., Massoth, G.J. and Baker, E.T. (1986) Bacterial scavenging of Mn and Fe in a mid-
815 to far-field hydrothermal particle plume. Nature 322, 169-171.
816
817 Cron, B.R., Sheik, C.S., Kafantaris, F.-C.A., Druschel, G.K., Seewald, J.S., German, C.R., Dick,
818 G.J., Breier, J.A. and Toner, B.M. (2020) Dynamic Biogeochemistry of the Particulate Sulfur
819 Pool in a Buoyant Deep-Sea Hydrothermal Plume. ACS Earth and Space Chemistry 4, 168-182.
820
821 Cutter, G.A. (2001) Metalloids and Oxyanions, in: Steele, J.H., Thorpe, S.A., Turekian, K.K.
822 (Ed.), Marine Chemistry and Geochemistry. Elsevier.
823
824 Drummond, S.E. (1981) Boiling and mixing of hydrothermal fluids: chemical effects on mineral
825 precipitation,, Pennsylvania State University, University Park, PA, .
826
827 Estapa, M.L., Breier, J.A. and German, C.R. (2015) Particle dynamics in the rising plume at
828 Piccard Hydrothermal Field, Mid-Cayman Rise. Geochemistry Geophysics Geosystems 16,
829 2762-2774.
830
831 Evans, G.N., Tivey, M.K., Seewald, J.S. and Wheat, C.G. (2017) Influences of the Tonga
832 Subduction Zone on seafloor massive sulfide deposits along the Eastern Lau Spreading Center
833 and Valu Fa Ridge. Geochimica Et Cosmochimica Acta 215, 214-246.
834
835 Feely, R.A., Gendron, J.F., Baker, E.T. and Lebon, G.T. (1994) Hydrothermal plumes along the
836 East Pacific Rise, 8°40 to 11°50: Particle distribution and composition. Earth Planet. Sci. Lett.
837 128, 19-36.
838
839 Feely, R.A., Lewison, M., Massoth, G.J., Rober-Baldo, G., Lavelle, J.W., Byrne, R.H., Damm,
840 K.L.V. and H C Curl, J. (1987) Composition and dissolution of black smoker particulates from
841 active vents on the Juan de Fuca Ridge. J. Geophys. Res. 92, 11347-11363.
842
843 Feely, R.A., Massoth, G.J., Baker, E.T., Cowen, J.P., Lamb, M.F. and Krogslund, K.A. (1990)
844 The effect of hydrothermal processes on midwater phosphorus distributions in the northeast
845 Pacific. Earth and Planetary Science Letters 96, 305-318.
846
847 Ferrini, V.L., Tivey, M.K., Carbotte, S.M., Martinez, F. and Roman, C. (2008) Variable
848 morphologic expression of volcanic, tectonic, and hydrothermal processes at six hydrothermal
849 vent fields in the Lau back-arc basin. Geochemistry Geophysics Geosystems 9.
850

851 Findlay, A.J., Estes, E.R., Gartman, A., Yucel, M., Kamyshny, A. and Luther, G.W. (2019) Iron
852 and sulfide nanoparticle formation and transport in nascent hydrothermal vent plumes. Nature
853 Communications 10.
854
855 Fitzsimmons, J.N. and Boyle, E.A. (2014) Assessment and comparison of Anopore and cross
856 flow filtration methods for the determination of dissolved iron size fractionation into soluble and
857 colloidal phases in seawater. Limnol. Oceanogr.: Methods 12, 244-261.
858
859 Fitzsimmons, J.N., John, S.G., Marsay, C.M., Hoffman, C.L., Nicholas, S.L., Toner, B.M.,
860 German, C.R. and Sherrell, R.M. (2017) Iron persistence in a distal hydrothermal plume
861 supported by dissolved-particulate exchange. Nature Geoscience 10, 195-201.
862
863 Gartman, A. and Findlay, A.J. (2020) Impacts of hydrothermal plume processes on oceanic metal
864 cycles and transport. Nature Geoscience 13, 396-402.
865
866 Gartman, A., Findlay, A.J., Hannington, M., Garbe-Schonberg, D., Jamieson, J.W. and
867 Kwasnitschka, T. (2019) The role of nanoparticles in mediating element deposition and transport
868 at hydrothermal vents. Geochimica Et Cosmochimica Acta 261, 113-131.
869
870 Gartman, A., Findlay, A.J. and Luther III, G.W. (2014) Nanoparticulate pyrite and other
871 nanoparticles are a widespread component of hydrothermal vent black smoker emissions.
872 Chemical Geology 366, 32-41.
873
874 German, C.R., Bennett, S.A., Connelly, D.P., Evans, A.J., Murton, B.J., Parson, L.M., Prien,
875 R.D., Ramirez-Llodra, E., Jakuba, M., Shank, T.M., Yoerger, D.R., Baker, E.T., Walker, S.L.
876 and Nakamura, K. (2008) Hydrothermal activity on the southern Mid-Atlantic Ridge:
877 Tectonically- and volcanically-controlled venting at 4-5 degrees S. Earth and Planetary Science
878 Letters 273, 332-344.
879
880 German, C.R., Casciotti, K.A., Dutay, J.-C., Heimburger, L.E., Jenkins, W.J., Measures, C.I.,
881 Mills, R.A., Obata, H., Schlitzer, R., Tagliabue, A., Turner, D.R. and Whitby, H. (2016)
882 Hydrothermal impacts on trace element and isotope ocean biogeochemistry. Philosophical
883 Transactions of the Royal Society A 374: 20160035.
884
885 German, C.R. and Seyfried, W.E., Jr (2014) Hydrothermal Processes, Treatise on Geochemistry.
886 Elsevier, pp. 191-233.
887
888 Govindarajan, A.F. (1994) Compilation of working values and sample description for 383
889 geostandards. Geostand. Geoanal. Res. 18, 1639–4488.
890
891 Hammersley, A.P., Svensson, S.O., Hanfland, M., Fitch, A.N. and Hausermann, D. (1996) Two-
892 dimensional detector software: From real detector to idealized image or two-theta scan. High
893 Press. Res. 14, 235-248.
894

Hansel, C.M., Benner, S.G., Neiss, J., Dohnalkova, A., Kukkadapu, R.K. and Fendorf, S. (2003) Secondary mineralization pathways induced by dissimilatory iron reduction of ferrihydrite under advective flow. Geochim. Cosmochim. Acta 67, 2977-2992.

Helgeson, H.C. (1969) Thermodynamics of hydrothermal systems at elevated temperatures and pressures. American Journal of Science 267, 729.

Helgeson, H.C.D., J. M.; Nesbitt, H. W.; Bird, D. K. (1978) Summary and critique of the thermodynamic properties of rock-forming minerals. American Journal of Science, 1-129.

Helgeson, H.C.K., D. H. (1974) Theoretical prediction of the thermodynamic behavior of aqueous electrolytes at high pressures and temperatures; I, Summary of the thermodynamic/electrostatic properties of the solvent. . American Journal of Science, 1089-1198.

Hoffman, C.L., Nicholas, S.L., Ohnemus, D.C., Fitzsimmons, J.N., Sherrell, R.M., German, C.R., Heller, M.I., Lee, J.-M., Lam, P.J. and Toner, B.M. (2018) Near-field iron and carbon chemistry of non-buoyant hydrothermal plume particles, Southern East Pacific Rise 15oS. Marine Chemistry 201, 183-197.

Jacobs, A.M., Harding, A.J. and Kent, G.M. (2007) Axial crustal structure of the Lau back-arc basin from velocity modeling of multichannel seismic data. Earth and Planetary Science Letters 259, 239-255.

Janecky, D.R. and Seyfried, W.E. (1984) Formation of massive sulfide deposits on oceanic ridge crests – incremental reaction models for mixing between hydrothermal solutions and seawater. Geochimica Et Cosmochimica Acta 48, 2723-2738.

Jiang, H.S. and Breier, J.A. (2014) Physical controls on mixing and transport within rising submarine hydrothermal plumes: A numerical simulation study. Deep-Sea Research Part I-Oceanographic Research Papers 92, 41-55.

Johnson, J.W., Oelkers, E.H. and Helgeson, H.C. (1992) SUPCRT92 - A softward package for calculating the standard molal thermodynamic properties of minerals, gases, aqueous species, and reactions from 1-bar to 5000-bar and 0-degrees-C to 1000-degrees-C. Computers & Geosciences 18, 899-947.

Klevenz, V., Bach, W., Schmidt, K., Hentscher, M., Koschinsky, A. and Petersen, S. (2011) Geochemistry of vent fluid particles formed during initial hydrothermal fluid-seawater mixing along the Mid-Atlantic Ridge. Geochemistry Geophysics Geosystems 12.

Lam, P.J., Lee, J.-M., Heller, M.I., Mehic, S., Xiang, Y. and Bates, N.R. (2018) Size-fractionated distributions of suspended particle concentration and major phase composition from the U.S. GEOTRACES Eastern Pacific Zonal Transect (GP16). Marine Chemistry 201, 90-107.

Lee, J.-M., Heller, M.I. and Lam, P.J. (2018) Size distribution of particulate trace elements in the U.S. GEOTRACES Eastern Pacific Zonal Transect (GP16). Marine Chemistry 201, 108-123.

941
942 Li, M., Toner, B.M., Baker, B.J., Breier, J.A., Sheik, C.S. and Dick, G.J. (2014) Microbial iron
943 uptake as a mechanism for dispersing iron from deep-sea hydrothermal vents. Nature
944 Communications 5.
945
946 Lough, A.J.M., Connelly, D.P., Homoky, W.B., Hawkes, J.A., Chavagnac, V., Castillo, A.,
947 Kazemian, M., Nakamura, K., Araki, T., Kaulich, B. and Mills, R.A. (2019) Diffuse
948 Hydrothermal Venting: A Hidden Source of Iron to the Oceans. Frontiers in Marine Science 6.
949
950 Marcus, M.A., MacDowell, A., Celestre, R., Manceau, A., Miller, T., Padmore, H.A. and
951 Sublett, R.E. (2004) Beamline 10.3.2 at ALS: a hard X-ray microprobe for environmental and
952 material sciences. J. Synchrotron Rad. 11, 239-247.
953
954 Marcus, M.A., Westphal, A.J. and Fakra, S. (2008) Classification of Fe-bearing species from K-
955 edge XANES data using two-parameter correlation plots. J Synchrotron Rad. 15, 463-468.
956
957 Martinez, F., Taylor, B., Baker, E.T., Resing, J.A. and Walker, S.L. (2006) Opposing trends in
958 crustal thickness and spreading rate along the back-arc Eastern Lau Spreading Center:
959 Implications for controls on ridge morphology, faulting, and hydrothermal activity. Earth and
960 Planetary Science Letters 245, 655-672.
961
962 Mayhew, L.E., Webb, S.M. and Templeton, A.S. (2011) Microscale imaging and identification
963 of Fe oxidation state, speciation, and distribution in complex geological media. Environmental
964 Science & Technology 45, 4468-4472.
965
966 McCollom, T.M. (2000) Geochemical constraints on primary productivity in submarine
967 hydrothermal vent plumes. Deep-Sea Res. 47, 85-101.
968
969 McCollom, T.M. and Shock, E.L. (1997) Geochemical constraints on chemolithoautotrophic
970 metabolism by microorganisms in seafloor hydrothermal systems. Geochim. Cosmochim. Acta
971 61, 4375-4391.
972
973 Mottl, M.J. and McConachy, T.F. (1990) Chemical processes in buoyant hydrothermal plumes
974 on the East Pacific Rise near 21 ^{o} N. Geochim. Cosmochim. Acta 54, 1911-1927.
975
976 Mottl, M.J., Seewald, J.S., Wheat, C.G., Tivey, M.K., Michael, P.J., Proskurowski, G.,
977 McCollom, T.M., Reeves, E., Sharkey, J., You, C.F., Chan, L.H. and Pichler, T. (2011)
978 Chemistry of hot springs along the Eastern Lau Spreading Center. Geochimica Et Cosmochimica
979 Acta 75, 1013-1038.
980
981 Nicholas, S.L., Erickson, M.L., Woodruff, L.G., Knaeble, A.R., Marcus, M.A., Lynch, J.K. and
982 Toner, B.M. (2017) Solid-phase arsenic speciation in aquifer sediments: a micro-X-ray
983 absorption spectroscopy approach for quantifying trace-level speciation. Geochim Cosmochim
984 Acta 211, 228-255.
985 Ravel, B. and Newville, M. (2005) Athena, Artemis, Hephaestus: data analysis for X-ray
986 absorption spectroscopy using IFEFFIT. Journal of Synchrotron Radiation 12, 537-541.

Robie, R.A.H., B. S.; Fisher, J. R. (1979) Thermodynamic properties of minerals and related substances at 298.15 K and 1 Bar (10 Pascals) pressure and at higher temperatures. , US Geological Survey 1979, Bulletin p. 456.

Saccocia, P.J. and Seyfried, W.E. (1994) The solubility of chlorite solid solutions in 3.2 wt% NaCl fluids from 300–400°C, 500 bars. Geochimica et Cosmochimica Acta 58, 567-585.

Sander, S.G. and Koschinsky, A. (2011) Metal flux from hydrothermal vents increased by organic complexation. Nature Geoscience 4, 145-150.

Sander, S.G., Koschinsky, A., Massoth, G.J., Stott, M. and Hunter, K.A. (2007) Organic complexation of copper in deep-sea hydrothermal vent systems. Environ. Chem. 4, 81-89.

Seewald, J.M., T.; Proskurowski, G.; Reeves, E.; Mottl, M.; Sharkey, J.; Wheat, C. G.; Tivey, M. (2005) Aqueous volatiles in Lau Basin hydrothermal fluids, American Geophysical Union Fall Meeting, pp. T31A-0478.

Shafer, M.M., Toner, B.M., Overdier, J., Schauer, J.J., Fakra, S.C., Hu, S., Herner, J.D. and Ayala, A. (2011) Chemical speciation of vanadium in particulate matter emitted from diesel vehicles and urban atmospheric aerosols. Environmental Science & Technology 46, 189-195.

Sheik, C.S., Anantharaman, K., Breier, J.A., Sylvan, J.B., Edwards, K.J. and Dick, G.J. (2015) Spatially resolved sampling reveals dynamic microbial communities in rising hydrothermal plumes across a back-arc basin. ISME Journal 9, 1434-1445.

Shock, E.L. and Helgeson, H.C. (1990) Calculation of the thermodynamic and transport properties of aqueous species at high pressures and temperatures: Standard partial molal properties of organic species. Geochimica et Cosmochimica Acta 54, 915-945.

Shock, E.L., Helgeson, H.C. and Sverjensky, D.A. (1989) Calculation of the thermodynamic and transport properties of aqueous species at high pressures and temperatures: Standard partial molal properties of inorganic neutral species. Geochimica et Cosmochimica Acta 53, 2157-2183.

Shock, E.L., Sassani, D.C., Willis, M. and Sverjensky, D.A. (1997) Inorganic species in geologic fluids: Correlations among standard molal thermodynamic properties of aqueous ions and hydroxide complexes. Geochimica et Cosmochimica Acta 61, 907-950.

Speer, K.G. and Helfrich, K.R. (1995) Hydrothermal plumes: a review of flow and fluxes, in: Parson, L.M., Walker, C.L., Dixon, D.R. (Eds.), Hydrothermal Vents and Processes. Geological Society Special Publications, pp. 373-385.

Sverjensky, D.A., Shock, E.L. and Helgeson, H.C. (1997) Prediction of the thermodynamic properties of aqueous metal complexes to 1000°C and 5 kb. Geochimica et Cosmochimica Acta 61, 1359-1412.

Talley, L.D. (2007) Hydrographic atlas of the world ocean circulation experiment (WOCE) , in: Sparrow, M., Chapman, P. and Gould, J. (Ed.), Volume 2: Pacific Ocean, Southampton, UK.

Toner, B.M., Bennett, S.A., Chu, N.C. and German, C.R. (2009a) Deep ocean interactions between hydrothermally-sourced iron and organic carbon. Geochimica et Cosmochimica Acta 73, A1340-A1340.

Toner, B.M., Berquo, T.S., Michel, F.M., Sorensen, J.V., Templeton, A.S. and Edwards, K.J. (2012a) Mineralogy of iron microbial mats from Loihi Seamount. Frontiers in Microbiological Chemistry 3, 1-18.

Toner, B.M., German, C.R., Dick, G.J. and Breier, J.A. (2015) Deciphering the Complex Chemistry of Deep-Ocean Particles using Complementary Synchrotron X-ray Microscope and Microprobe Instruments. Accounts of Chemical Research 49, 128-137.

Toner, B.M., Lam, P.J., Nicholas, S.L., Ohnemus, D.C., Hoffman, C.L., Fitzsimmons, J.N., Sherrell, R.M. and German, C.R. (2014) The Speciation of Particulate Iron and Carbon in the East Pacific Rise 15ºS Near-field Hydrothermal Plume and Underlying Sediments, 2014 Fall Meeting, San Francisco, CA, USA.

Toner, B.M., Marcus, M.A., Edwards, K.J., Rouxel, O. and German, C.R. (2012b) Measuring the Form of Iron in Hydrothermal Plume Particles. Oceanography 25, 209-212.

Toner, B.M., Santelli, C.M., Marcus, M.A., Wirth, R., Chan, C.S., McCollom, T.M., Bach, W. and Edwards, K.J. (2009b) Biogenic iron oxyhydroxide formation at Mid-Ocean Ridge hydrothermal vents: Juan de Fuca Ridge. Geochim. Cosmochim. Acta 73, 388-403.

Von Damm, K.L., Edmond, J.M., Grant, B., Measures, C.I., Walden, B. and Weiss, R.F. (1985) Chemistry of submarine hydrothermal solutions at 21 °N, East Pacific Rise. Geochimica et Cosmochimica Acta 49, 2197-2220.

Wagman, D.D.E., W. H.; Parker, V. B.; Schumm, R. H.; Halow, I.; Balley, S., M.; Churney, K. L. (1982) NBS Tables of Chemical Thermodynamic Properties: Selected Values for Inorganic and C1 and C2 Organic Substances in SI Units. American Chemical Society and the American Institute of Physics for the National Bureau of Standards, Washington, D.C.

Yu, J.Y., Park, M. and Kim, J. (2002) Solubilities of synthetic schwertmannite and ferrihydrite. Geochemical Journal 36, 119-132.

Yucel, M., Gartman, A., Chan, C.S. and George W. Luther, I. (2011) Hydrothermal vents as a kinetically stable source of iron-sulphide-bearing nanoparticles to the ocean. Nature Geoscience 4, 367-371.

Zeng, T., Arnold, W.A. and Toner, B.M. (2013) Microscale characterization of sulfur speciation in lake sediments. Environmental Science & Technology 47, 1287-1296.

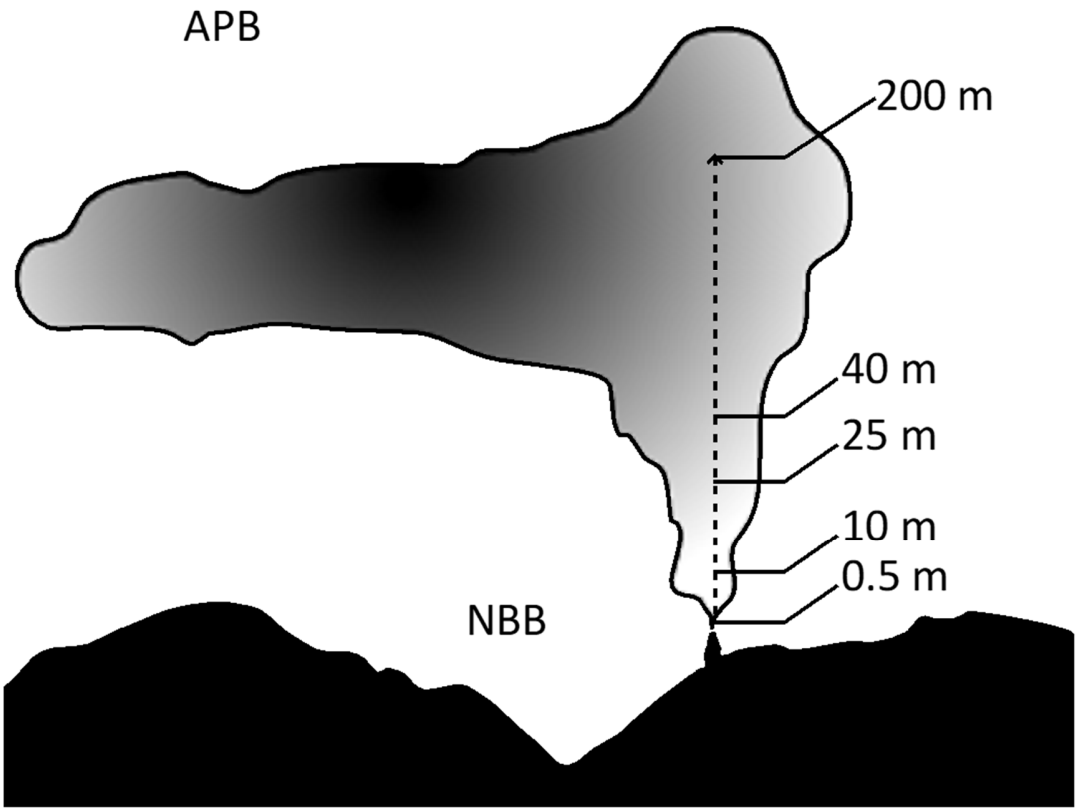

Figure 1. Schematic of buoyant hydrothermal plume showing plume elevation (in meters) and approximate location of sampling at ABE vent field, including the near bottom background (NBB) and above plume background (APB).

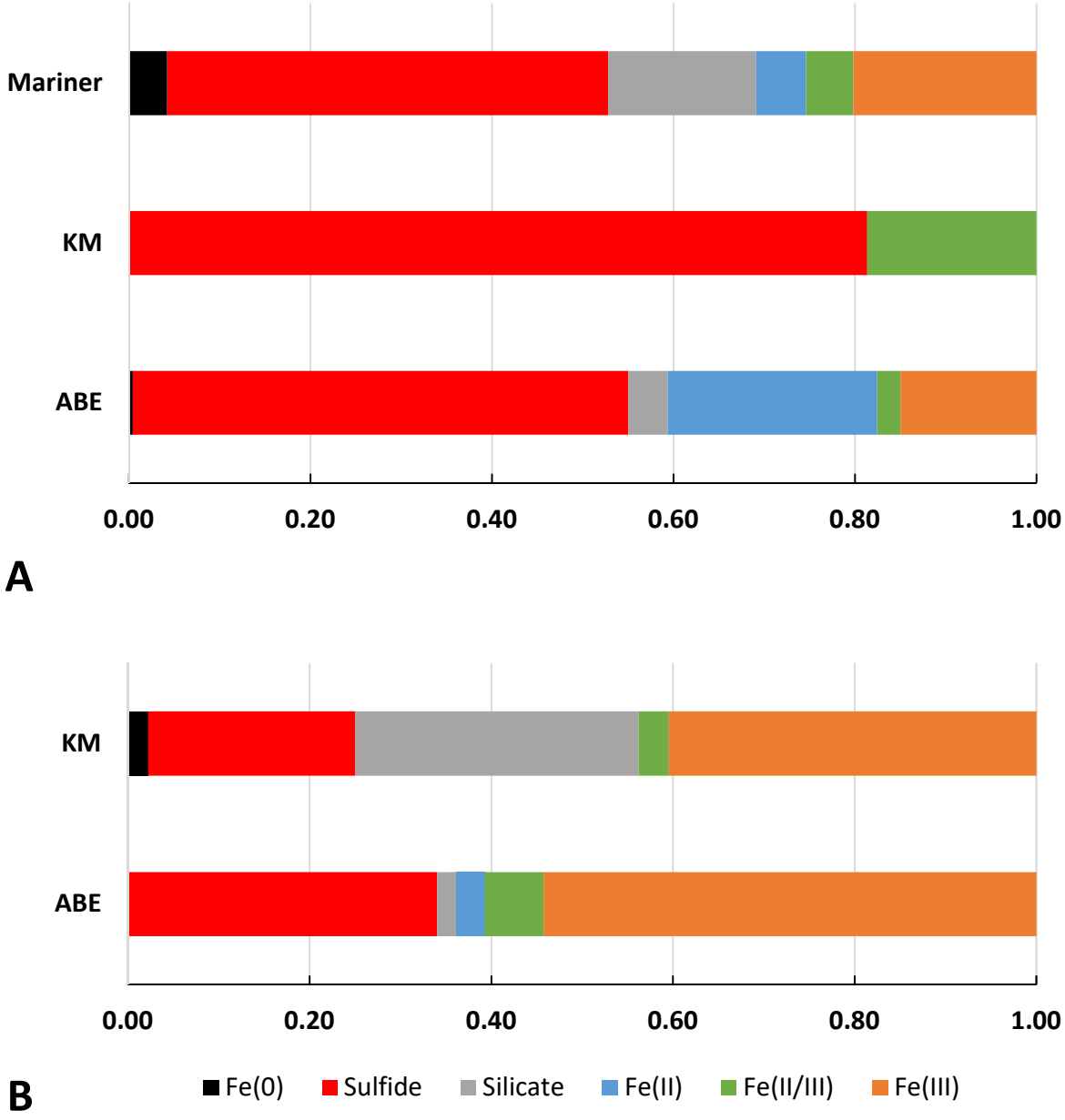

Figure 2: Results from point X-ray absorption near edge structure (XANES) spectra showing difference in particulate Fe speciation between locations, the Kilo Moana, ABE, and Mariner vent fields, for a given plume elevation. A) 0.5/1.5 m and B) 200m above the vent and within the buoyant plume.

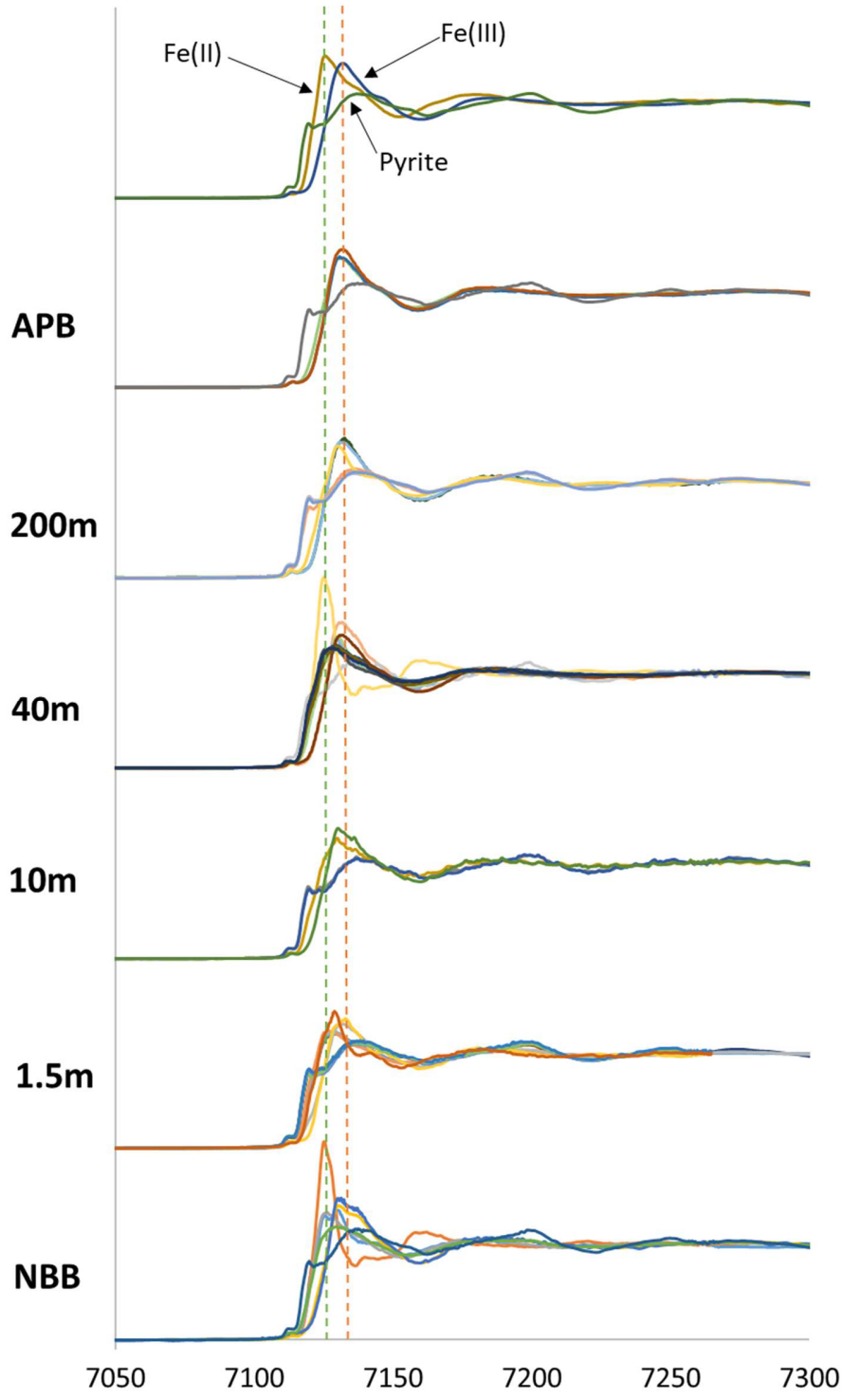

Figure 3: Iron point X-ray absorption near edge structure (XANES) spectra showing differences in particulate Fe speciation for samples collected as the above plume background (APB), within the buoyant plume at different elevations above the vent, and a near bottom background (NBB) for an ABE vent. Green and orange dotted lines represent the position of Fe(II) and Fe(III) spectra, respectively.

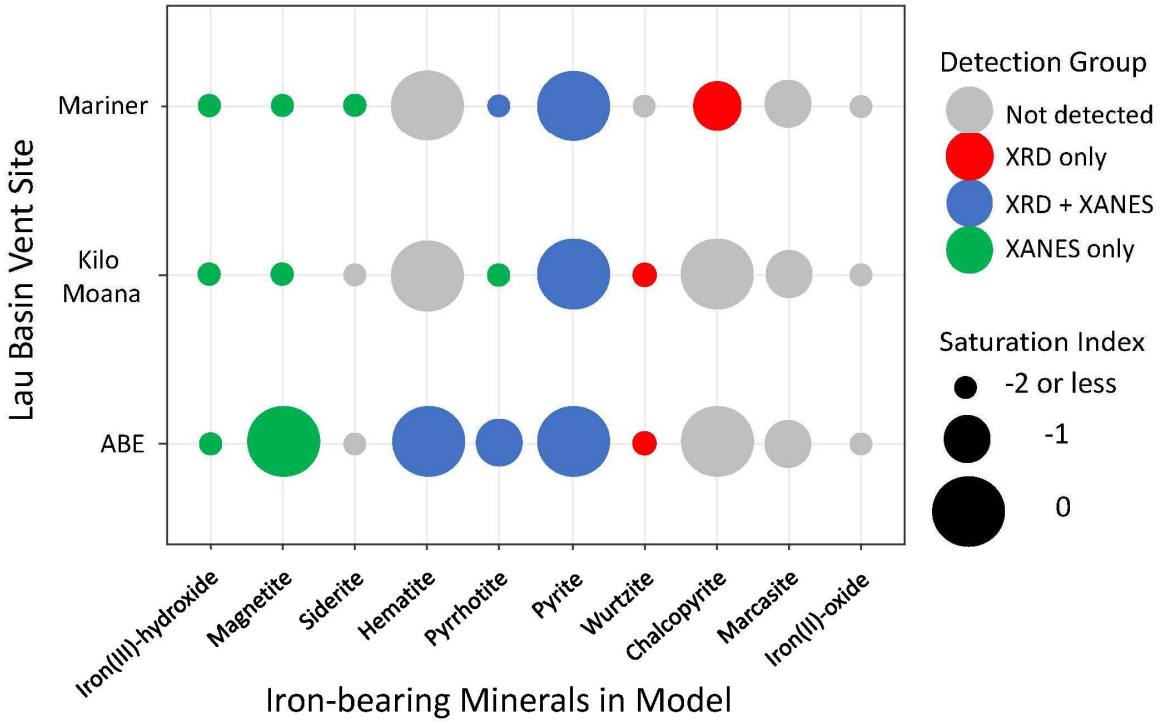

Figure 4. Bubble plot showing the detection mode (by color) and thermodynamic model saturation index (SI, by circle size) for Fe-bearing minerals included in the thermodynamic database according to vent field. Detection modes are: (1) not detected, ND, in grey; (2) X-ray diffraction, XRD, in red; (3) X-ray absorption near edge structure, XANES, spectroscopy, in green; and (4) both XRD and XANES in blue. The saturation index (SI) is represented by: (1) largest circles have an SI = 0, and are predicted to form in the plume by the model; and (2) smaller circles have an SI of -1 or -2 and are not predicted to form in the plume by the model.

Table 1. Proportion of Fe-Sulfide, Fe(II) and Fe(III) for all sampling locations and plume elevations based on chemical mapping measurements.

Vent Field	Buoyant Plume Location	Plume Elevation (m)	Proportion Fe-Sulfide	Proportion Fe(II)	Proportion Fe(III)	pFe (nmol Fe/kg seawater)[c]	Temp (deg C)
ABE	NBB[a]	0	0.40	0.08	0.52	10.6	309.00
ABE	1.5m	1.5	0.52	0.14	0.33	18.9	
ABE	10m	10	0.13	0.09	0.78	4.21	
ABE	40m	40	0.36	0.13	0.51	3.16	
ABE	200m	200	0.54	0.07	0.39	3.86	
ABE	APB[b]	300	0.05	0.04	0.91	1.06	
Kilo Moana	NBB	0	0.23	0.06	0.71	18	333.00
Kilo Moana	0.5m	0.5	0.35	0.11	0.54	35.8	
Kilo Moana	200m	200	0.15	0.10	0.74	3.16	
Kilo Moana	APB	300	0.15	0.33	0.52	3.81	
Mariner	0.5m	0.5	0.03	0.08	0.87	204	334.00
Mariner	25m	25	0.24	0.27	0.48	10.5	

a) Near bottom background

b) Above plume background

c) Total particulate Fe concentration (pFe) was measured by ICP-OES after digestion of filter solids

Table 2. Results from X-ray diffraction (XRD) and Fe X-ray absorption near edge structure (XANES) spectroscopy detection at all three vent sites. Minerals underlined are predicted to form by geochemical modeling.

	Formula	Detection Mode by Site		
Metal Sulfides & Elemental Sulfur		**Kilo Moana**	**ABE**	**Mariner**
Bornite	Cu_5FeS_4	XRD	-	-
Chalcocite	Cu_2S	-	XRD	-
Chalcopyrite	$CuFeS_2$	-	-	XRD
Cubanite	$CuFe(II)_2S_3$	-	XANES	XANES
Iron Titanium Sulfide	$FeTi_3S_6$	-	-	XRD
Kesterite	$Cu_2(Zn,Fe)SnS_4$	XRD	-	-
Lautite	CuAsS	XRD	XRD	-
Mackinawite	$(Fe,Ni)_{(1+x)}S$; (x=0-0.11)	-	-	XANES
Pentlandite	$(Fe_xNi_y)_{(x+y)}S_8$; x+y=9	-	XANES	XANES
Pyrite	FeS_2	XRD,XANES	XRD,XANES	XRD,XANES
Pyrrhotite	$Fe_{(1-x)}S$; x=0-0.17	XANES	XANES	XANES
Rudashevskyite	(Fe,Zn)S	XRD	-	-
Sphalerite	(Zn, Fe)S	-	XRD	XRD
Stannoidite	$Cu(I,II)_8(Fe(II),Zn)_3Sn_2S_{12}$	XRD	-	-
Troilite or FeS	FeS	XANES	XRD,XANES	XANES
Wurtzite	(Zn, Fe)S	XRD	XRD	-
Elemental Sulfur	S8	-	XRD	XRD
Metal (Oxyhydr)oxides				
Akaganeite	β-FeO(OH,Cl)	-	XANES	-
Biogenic Iron Oxyhydroxide (formula unknown)		-	XANES	XANES
Chromite	$Fe(II)Cr(III)_2O_4$	-	XANES	XANES
Ferrihydrite	$Fe_2O_{3-0.5y}(OH)_y \cdot nH_2O$ y=0-1.96; n=0.82-1.14	XANES	XANES	XANES
Franklinite	$(Fe,Zn)_2O_4$	-	-	XRD
Goethite	α-FeOOH	XANES	XANES	XANES
Green Rust	$Fe(III)_xFe(II)_y(OH)_{3x+2y-z}(A^-)_z$; $A^-=Cl^-$; $0.5SO_4^{2-}$	XANES	XANES	XANES
Hematite	Fe_2O_3	-	XRD,XANES	-
Ilmenite	$Fe(II)TiO_3$	-	-	XANES
Lepidocrocite	γ-FeOOH	-	-	XANES
Magnetite	$Fe(II,III)_3O_4$	XANES	XANES	XANES
Perovskite	$(Ca,Fe)TiO_3$	-	XANES	XANES
Pseudobrookite	$Fe(III)_2Ti(IV)O_5$	XANES	XANES	XANES
Wustite	FeO	-	-	XANES
Sulfates, Phosphates, Carbonates & Halides				
Apatite	$Ca_5(PO_4)_3(Cl/F/OH)$	-	-	XRD
Coalingite	$Mg_{10}Fe(III)_2(OH)_{24}CO_3 \cdot 2H_2O$	-	XANES	XANES
Fluorite	CaF_2	-	-	XRD
Grattarolaite	$Fe_3(PO_4)O_3$	-	-	XRD
Halite	NaCl	-	XRD	XRD
Iron Sulfate	$FeSO_4$	-	XANES	XANES
Molysite	$FeCl_3$	-	XANES	XRD
Schulenbergite	$(Cu,Zn)_7(SO_4)_2(OH)_{10} \cdot 3H_2O$	-	XRD	XRD
Siderite	$FeCO_3$	-	-	XANES
Silicates				
Grossular	$Ca_3Al_2(SiO_4)_3$	-	XRD	-
Akermanite	$Ca_2Mg(Si_2O_7)$	-	XRD	-
Quartz	SiO_2	-	XRD	-
Ferrosmectite	Ferruginous Smectite Swa-1[a]	XANES	-	XANES
Montmorillonite	Texas Montmorillonite STx-1[a]	-	XANES	XANES
Nontronite	Nontronite NG-1[b]	-	XANES	-
Richterite	$Na(NaCa)Mg_5Si_8O_{22}(OH)_2$	XANES	XANES	XANES
Roedderite	$Na_{1.5}K_{0.5}Mg_{3.75}Fe(II)_{1.25}Si_{12}O_{30}$	XANES	XANES	-
Augite	$(Ca,Na)(Mg,Fe,Al,Ti)(Si,Al)_2O_6$	XANES	XANES	XANES
Almandine	$Fe(II)_3Al_2(SiO_4)_3$	-	XANES	XANES
Hypersthene	$(Mg,Fe)SiO_3$	XANES	XANES	-
Chlorite	$(Mg,Fe)_3(Si,Al)_4O_{10}(OH)_2 \cdot (Mg,Fe)_3(OH)_6$	-	XANES	-
Olivine	$(Mg,Fe)SiO_4$	-	XANES	XANES
Gehlenite	$Ca_2Al(AlSiO_7)$	-	-	XANES
Hedenbergite	$CaFe(II)Si_2O_6$	-	-	XANES

Phases in *italic* are predicted equilibrium phases (SI=0) while phases that are underlined are predicted to be undersaturated (0>SI>-2).

a) Clay Minerals Society source clays